LESSONS LEARNED FROM SUPERSONIC RETROPROPULSION WIND TUNNEL TESTING AND COMPUTATIONAL ANALYSIS

Karl T. Edquist

NASA Langley Research Center, Hampton, Virginia, USA

ABSTRACT

Testing was completed in the NASA Langley Unitary Plan Wind Tunnel to investigate aerodynamic interference on sub-scale Mars powered descent vehicle concepts at Mach numbers of 2.4 to 4.6: a model of a blunt hypersonic inflatable aerodynamic decelerator (HIAD) and the other representing a slender vehicle with body flaps (CobraMRV). Measurements included high-speed video, discrete pressures, and pressure sensitive paint. High-speed imagery revealed an unsteady plume/shock interaction for certain thrust levels and model attitudes, resulting in unsteady pressures on the model heatshields. Computational flowfield predictions of varying fidelity were completed using three solvers, and were compared to the test data. Qualitatively, the predicted gross flowfield features compare well to the high-video imagery. Overall, the computed heatshield pressure coefficients are consistent between solvers and follow the trends revealed in the time-averaged data. More advanced turbulence modeling methods are able to capture highly-unsteady pressures measured on certain models at some conditions. The test data will continue to be used to guide future testing investments and best practices for computational methods.

Index Terms— Supersonic Retropropulsion, NASA Langley Unitary Plan Wind Tunnel, Computational Fluid Dynamics

1. INTRODUCTION

Over the past several years, NASA engineers have investigated new technologies for Mars entry, descent, and landing (EDL) to enhance or enable delivering payloads that are much larger than is currently possible [1]. An enabling technology is the use of retrorockets, starting at supersonic conditions (supersonic retropropulsion = SRP), in place of a parachute for payloads larger than approximately five metric tons. Supersonic parachutes have been used for all NASA successful Mars landings, but they are not scalable for human exploration payloads (approximately 20 metric tons). Powered descent has been successfully completed at Mars subsonic conditions, but never at supersonic speeds where interactions between the exhaust plumes and surrounding flowfield cause unknown aerodynamic interference forces and moments. Currently, there is limited experience in using computational fluid dynamics (CFD) methods to predict the static aerodynamic loads on Mars powered descent vehicles [2]. CFD uncertainties must be further investigated for SRP aero/propulsive interactions, given how significantly they will factor into the overall EDL risk for landing larger Mars payloads.

Two NASA Mars high-mass entry system concepts (approximately 20 metric ton payloads) and reference trajectories are shown in Figure 1. The first reference vehicle is based on a Hypersonic Inflatable Aerodynamic Decelerator (HIAD, 16.4-meter diameter) aeroshell. The second reference vehicle, the Co-Optimization Blunt-body Re-entry Analysis-Mid-lift-to-drag Rigid Vehicle (CobraMRV, 22-meter length), is a slender rigid aeroshell with body flaps and can generate more lift than the HIAD. Both EDL sequences powered descent starting at supersonic conditions using eight engines, each producing a maximum of 100 kN of thrust. The powered flight segment starts at Mach numbers above 2 and ends with a soft landing within 50 meters of the target [1].

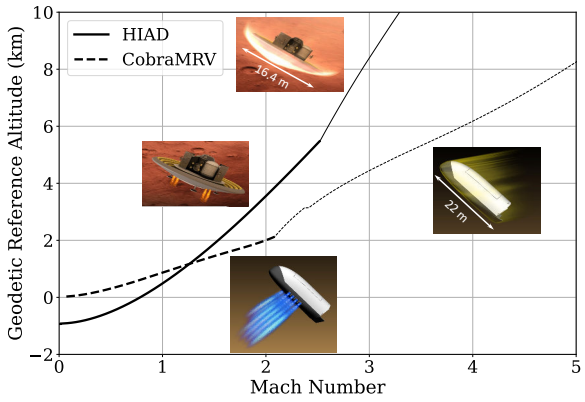

Fig. 1: Mars entry vehicle concepts and reference trajectories. Thick lines indicate powered descent.

Testing was conducted at NASA Langley Research Center to provide a SRP data set against which CFD methods can be calibrated for accuracy. Previous papers [3, 4, 5, 6] provide detailed overviews of the test campaign and CFD analysis. This paper summarizes lessons learned from the wind tunnel test data and CFD analysis. The test results are shown along with available CFD solver results, focusing on discrete and global pressures on the heatshield, and aerodynamic force data derived from the pressure data.

2. TEST FACILITY

The test was conducted in the NASA Langley Research Center Unitary Plan Wind Tunnel (LUPWT), a closed-circuit continuous-flow pressure tunnel with two test sections that each have a nominal four-feet square cross section. The Mach number ranges are 1.50 to 2.86 in Test Section 1 and 2.30 to 4.63 in Test Section 2. The SRP test was conducted in Test Section 2 (Figure 2), the same section that was used for a similar test in 2010 [7]. The Mach number in the test section is controlled by an asymmetric sliding-block nozzle, which is used to select the nozzle area ratio. A re-characterization of Test Section 2 was completed in 2020; the data confirmed non-uniform Mach number and dynamic pressure distributions, and non-zero flow angularity [8]. The updated tunnel conditions used for the test are in Table 1: Mach number (M_∞), total temperature (T_0), Reynolds number (Re_∞), and dynamic pressure ($\bar{q}$).

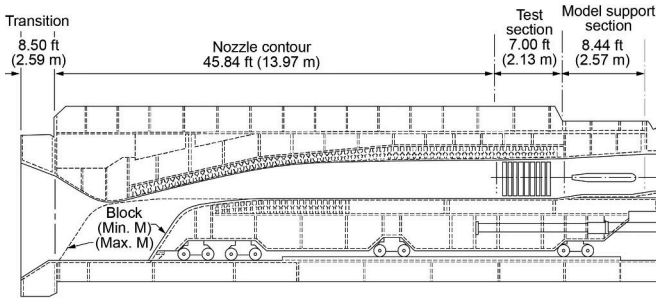

Fig. 2: NASA LUPWT Test Section 2.

Table 1: Wind tunnel reference conditions.

Condition	M_∞	T_0 (°F)	Re_∞/ft (10^6)	$\bar{q}$ (lb_f/ft^2)
5	2.386	125	1	210.34
20	3.477	125	1	153.22
35	4.568	150	1.5	167.41

3. WIND TUNNEL MODELS

The wind tunnel environment is different from conditions at Mars in a number of ways, including the freestream gas (air in the tunnel versus CO_2 at Mars), the Mach and Reynolds numbers, and the plume gases: high pressure air (HPA) in the tunnel versus hot combustion products in flight. With that in mind, the wind tunnel models were designed to be as relevant as possible to NASA human-scale Mars flight reference vehicles. First, the heatshield outer mold lines were geometrically scaled from the ideal flight geometries. Second, the simulated engine nozzle exit locations for some models were placed on the heatshields at the same locations that have been modeled at Mars flight conditions on both concepts [2]. Third, some of the HIAD models and the single CobraMRV model had nozzle exit areas that are the same, relative to the heatshield area, as the flight concepts. The major difference in the nozzles is the required model exit-to-throat area ratio (A_e/A_t), which is limited by the desire to avoid expansion of HPA to extremely low temperatures outside of the nozzle, and possible multi-phase flow. Whereas the flight nozzles will likely have very high area ratios above 100, the model area ratios were 4:1 (isentropic exit Mach number of about 2.94) and 11:1 (smaller throat, Mach number of 4.03).

Figure 3 summarizes the heatshields of the blowing models tested. All nozzles had 15° half-angle conical convergent and divergent sections, with a short straight section for the throat. The nozzle exits were scarfed to follow the heatshield surface contour, making some nozzle/heatshield interfaces non-circular. The HIAD model was designed to explore some key parameters that were expected to influence the results, using interchangeable nozzle inserts. Nozzle location on the heatshield (R_n/R_b), nozzle pointing direction (θ_{cant}) relative to the horizontal in the figure inset, and nozzle area ratio all were varied in the HIAD model. Figure 4 shows HIAD model 1A and CobraMRV model 2A installed on the sting prior to testing.

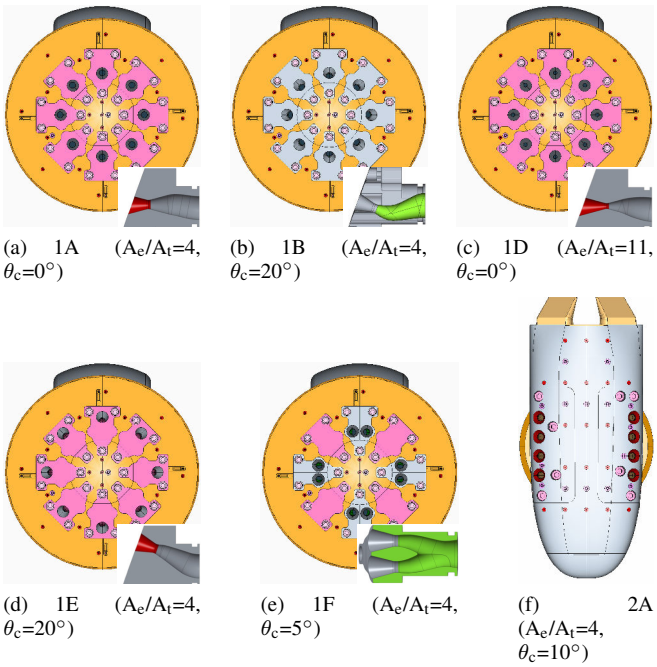

(a) 1A (A_e/A_t=4, θ_c=0°) (b) 1B (A_e/A_t=4, θ_c=20°) (c) 1D (A_e/A_t=11, θ_c=0°)

(d) 1E (A_e/A_t=4, θ_c=20°) (e) 1F (A_e/A_t=4, θ_c=5°) (f) 2A (A_e/A_t=4, θ_c=10°)

Fig. 3: Blowing wind tunnel models: HIAD (1A through 1F) and CobraMRV (2A).

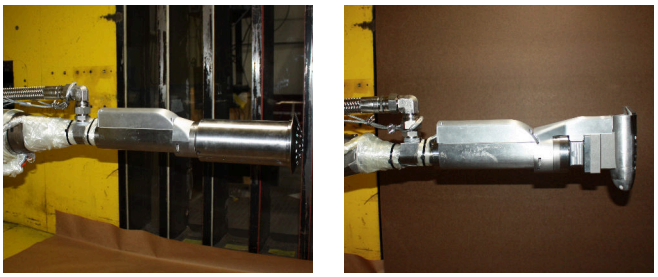

(a) HIAD model 1A (b) CobraMRV model 2A

Fig. 4: Installed models.

4. TEST MEASUREMENTS

The test included the same types of measurements that were collected in the 2010 UPWT SRP test [7], in addition to new measurement techniques aimed specifically at the SRP problem. High-speed video was used to investigate the qualitative impact of the various test parameters on the complex SRP flowfield. Static and unsteady pressure were measured at discrete locations on the external model surfaces, to determine the impact of SRP on heatshield pressure and compare to CFD predictions. Finally, pressure sensitive paint (PSP) was used to provide steady pressure distributions on the heatshields, a technique that was not used in 2010. Direct measurement of forces and moments also was attempted using a custom flow-through balance [9] that was designed and manufactured after the models were fabricated. However, no usable data were obtained, likely due to unforeseen balance sensitivity to temperature drift [3].

4.1. High-Speed Schlieren Video

A Photron NOVA S12 camera was used to acquire video at a resolution of 1024 by 1024 pixels. Capture rates of 3000 to 10,000 frames

per second were used with a 10^{-5}-second shutter speed. The camera was synchronized to a time signal to allow for cross reference with time signatures on acquired data. The videos provided detailed qualitative information about the highly unsteady flowfield induced by the bow shock and HPA exhaust plume interaction.

4.2. Discrete Pressures

Static pressure sensors (taps) were installed on both models (30 on the HIAD model and 29 on CobraMRV) to measure steady pressures. Figure 5 shows the measurement locations on the front of each model heatshield. The taps were connected to a 15-psia 32-port miniature electronically-scanned pressure (ESP) module located inside the model. Data from the pressure scanner were recorded at 10 Hz. Unsteady surface pressure was measured using 25-psia Kulite® pressure transducers (Kulites), 14 on the HIAD model and 15 on the CobraMRV model, at a rate of 20 kHz.

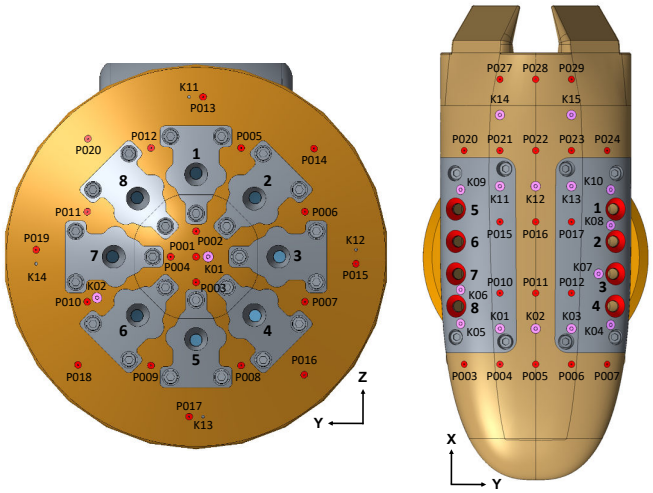

(a) HIAD (model 1A) (b) CobraMRV (model 2A)

Fig. 5: Nozzle numbers and heatshield pressure measurement locations (P = static taps, K = Kulites).

4.3. Pressure Sensitive Paint

PSP was applied to the model heatshields in order to provide quantitative steady-state pressure distributions. The setup included eight charge-coupled device cameras (2048 pixels by 2048 pixels) operating at 12-bit digital resolution. The PSP images were mapped to the model surface grid by using the known locations of registration marks in each image. The PSP data were corrected using static tap measurements, whereby regions of PSP near each tap were adjusted to minimize differences between the tap and PSP pressures, using a linear fit equation. The equation was used to adjust the pressure over the entire surface, which typically produced a coefficient of determination (R^2) higher than 0.9. However, there are certain conditions where the R^2 value was significantly less than 0.9, typically at higher jet blowing pressures (above 104 psia) and during angle of sideslip sweeps. Likely reasons for the reduced R^2 value are paint damage during model changes or uneven surface temperatures caused by complex interactions of the plumes with the surface. In these cases, the R^2 values would decrease to about 0.8 with a few cases approaching 0.7. In contrast, almost all of the data for non-blowing models had R^2 values of at least 0.9.

5. TEST DATA AND CFD ANALYSIS

Over 6300 test points were completed at combinations of tunnel Mach number (M_∞), model thrust coefficient (C_T = Thrust / $\bar{q}$S, $\bar{q}$ = dynamic pressure, S = reference area), and model angles of attack (α), sideslip (β), and roll (ϕ). The HIAD model variations were tested at angles of attack generally between -10° and 10°, where 0° is defined when the nominal velocity vector is aligned with the sting. The CobraMRV models were tested at α between 80° and 100°, where 90° is defined when the velocity vector is aligned with the sting. It was not possible to have both high-speed video and PSP at the same time; when PSP was started midway through the test, the matrix included repeat runs at conditions that were previously tested with high-speed video.

Three CFD solvers were used to simulate the models in the LUPWT environment: OVERset grid FLOW solver (OVERFLOW = OF, overset structured grids with mesh refinement), Fully Unstructured Navier-Stokes Three-Dimensional (FUN3D = F3, unstructured grids with mesh refinement), and LOCI-CHEM (LC, unstructured grids). All three solvers are commonly used for NASA missions, including for applications involving jet interactions. The CFD solutions included the tunnel walls, given that the test section is known to be non-uniform. The CFD inflow plane was taken from separate solutions of the tunnel settling chamber, nozzle, and test section. Results are shown for both time-accurate unsteady Reynolds-Averaged Navier-Stokes (URANS) simulations and higher-fidelity detached eddy simulations (DES). Details on the setup and results for each solver can be found in the literature [4, 5, 6].

More than 450 CFD calculations were completed using established best practices for grid generation, turbulence model settings, time-step requirements for unsteady solutions, and grid sensitivity studies. Most CFD solutions were completed prior to the test, with the CFD HPA total pressure values specified to achieve thrust coefficients of 0.5, 1, and 2.5 based on quasi one-dimensional isentropic compressible theory. Those same values were used as the HPA set point in the test matrix. However, due to losses in the HPA system, the resulting thrust coefficients were slightly lower than the theoretical values by 1.5% to 4%. Therefore, the plots shown in this paper include the calculated thrust coefficient based on isentropic theory, using the measured model flow path total pressure. C_T values higher than ≈3 (close to the initial flight values) during the test were attempted, but resulted in excessive tunnel wall interference.

5.1. High-Speed Schlieren Video

Qualitative observations of the flowfield structure were based on high-speed video, which reveals density gradients in the flowfield. The primary effect of SRP on the flowfield is that the nozzle plumes alter the shock layer, and thus the pressure distribution on the heatshield surfaces, by obstructing the far-field flow from cleanly reaching the model. This interference effect is highly dependent on the model/nozzle configuration, nozzle thrust, freestream Mach number, and model attitude. Figure 6 shows instantaneous images from non-blowing and blowing (at $C_T \approx 1$) HIAD models at a Mach number of 2.386. The black bars in each image are bars in the test section window. The gross effect of the nozzle plumes is to increase the size of the shock layer and to disturb the flow, sometimes extensively and in a very unsteady manner as will be seen in the pressure data. Model 1B and 1E have nozzles that canted (perpendicular to the heatshield surface), resulting in flatter bow shocks with smaller standoff distances in front of the heatshield compared to model 1A; the effect on measured heatshield pressure will be shown in the next section.

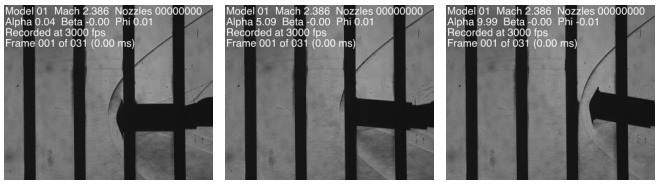

(a) Model 1, $\alpha = 0°$ (b) Model 1, $\alpha = 5°$ (c) Model 1, $\alpha = 10°$

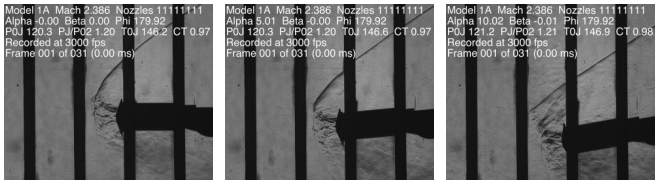

(d) Model 1A, $\alpha = 0°$ (e) Model 1A, $\alpha = -5°$ (f) Model 1A, $\alpha = -10°$

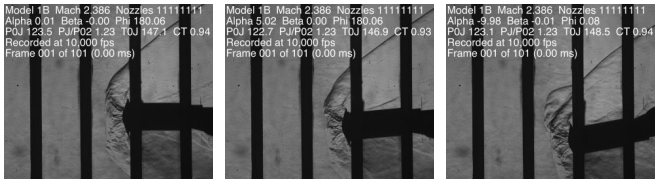

(g) Model 1B, $\alpha = 0°$ (h) Model 1B, $\alpha = -5°$ (i) Model 1B, $\alpha = -10°$

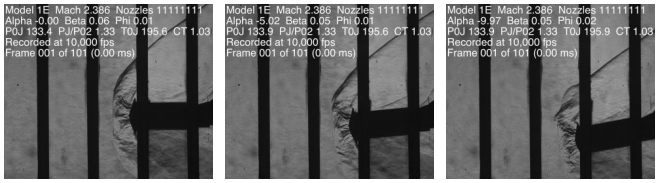

(j) Model 1E, $\alpha = 0°$ (k) Model 1E, $\alpha = -5°$ (l) Model 1E, $\alpha = -10°$

Fig. 6: Schlieren images of HIAD models ($C_T \approx 1$ for blowing models) at $M_\infty = 2.386$.

Figures 7 through 9 compare schlieren images with vorticity contours in the pitch plane from both DES and URANS solutions. At a model 1A thrust coefficient of 1, the solvers generally agree on the gross bow shock geometry, but with flatter shapes than was observed. However, the main drawback in using URANS for this problem is illustrated by the non-dimensional vorticity. The LOCI-CHEM URANS solutions indicate that excessive vorticity is produced everywhere behind the bow shock, multiple orders or magnitude higher than in the FUN3D DES solutions, due to artificially high viscosity. At the higher thrust coefficient of 2.5, the differences between DES and URANS are magnified, as shown in [4]. OVERFLOW DES solutions are included in the following results sections, and are discussed in more detail elsewhere [5, 6].

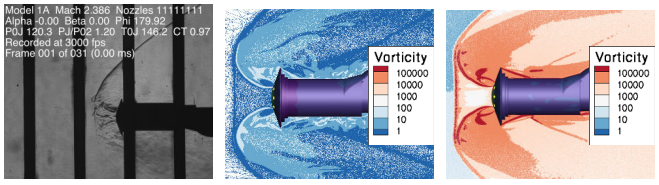

(a) Test (b) F3 DES (c) LC URANS

Fig. 7: Schlieren and CFD vorticity contours (s^{-1}) for model 1A at $M_\infty = 2.386$, $\alpha = 0°$, $C_T = 1$.

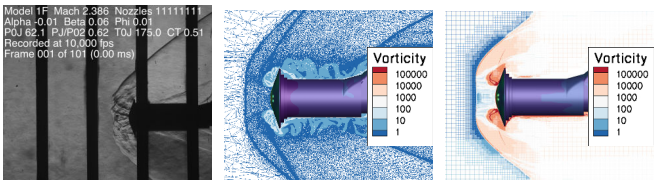

(a) Test (b) F3 DES (c) OF URANS

Fig. 8: Schlieren and CFD vorticity contours (s^{-1}) for model 1F at $M_\infty = 2.386$, $\alpha = 0°$, $C_T = 0.5$.

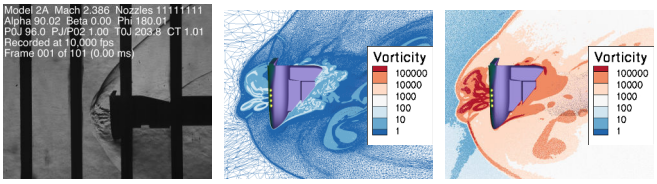

(a) Test, side view (b) F3 DES, side view (c) LC URANS, side view

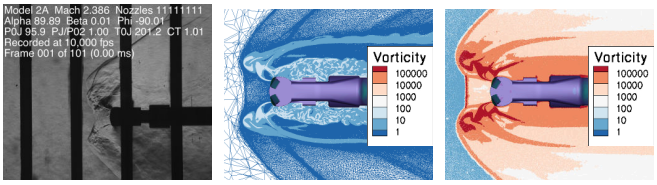

(d) Test, rear view (e) F3 DES, rear view (f) LC URANS, rear view

Fig. 9: Schlieren and CFD vorticity contours (s^{-1}) for model 2A at $M_\infty = 2.386$, $\alpha = 90°$, $C_T = 1$.

5.2. Discrete Pressures

The source of SRP aerodynamic interference is the altered heatshield surface pressure distribution due to complex physics happening between the plume exhaust and bow shock layer. Discrete pressure measurements from the wind tunnel test allow a quantitative assessment of CFD pressures on the model heatshields. All CFD results are presented as time-averaged values with one standard deviation ($\pm\sigma$) error bars. Both the static tap (steady) and Kulite (unsteady) data are shown. Kulite error bars that are shown in the plots are the unsteady $\pm\sigma$ values over approximately 40,000 data points taken at 20 kHz. The pressure data from some Kulites are not shown because of periodic data quality issues.

Figure 10 through Figure 15 shows pressure coefficient (C_p) on a subset of the models at or near the middle of the heatshield. Both static tap and Kulite data are shown for HIAD model 1A to illustrate pressure unsteadiness on the spherical nose. All repeat run data are shown on the plots. The effects of different HIAD nozzle parameters are illustrated by comparing models: nozzle cant angle (1A and 1B), nozzle radial location (1A and 1E), and nozzle clustering (1A and 1F). Each figure contains results at the reference attitude (middle plot) and +/-10° α or β (model 2A) excursions. Symbol colors indicate the ratio of the nozzle exit pressure (p_j) divided by the total stagnation pressure ($p_{0,2}$); for a given number of blowing nozzles, C_T is directly proportional to p_j / $p_{0,2}$. On model 1A, the static C_p is symmetric for positive and negative α, due to the symmetry of the model, the nozzles, and the tap location. The static tap and Kulite are located in close proximity to each other, so the average Kulite C_p is nearly equal to the static tap C_p. In general, the trend is that C_p stays at or above non-blowing values until the C_p reaches a level that

depends on the tunnel Mach number, model attitude, and number of blowing nozzles (4 or 8). At the highest thrust levels, the C_p is near zero, meaning that the contribution to aerodynamic force is insignificant. The transition from higher to lower C_p with 8 blowing nozzles is rapid. A more gradual decrease occurs with 4 nozzles (1, 3, 5, 7), where twice the p_j / $p_{0,2}$ is needed to reach a given C_T, resulting in more nozzle jet expansion and overall interference. There are some intermediate thrust levels where C_p is higher at a M_∞ of 3.477 versus 2.386. Finally, the C_p standard deviation error bars on the Kulite data indicate that pressure oscillations are influenced by model attitude (higher oscillations at off-reference attitudes) and thrust level (larger oscillations at lower thrust), especially at a M_∞ of 3.477.

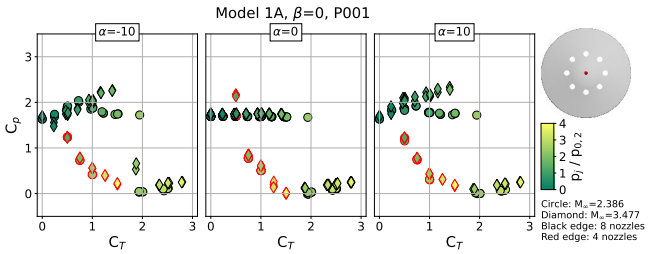

Fig. 10: Model 1A static tap C_p at heatshield center at $\beta = 0°$.

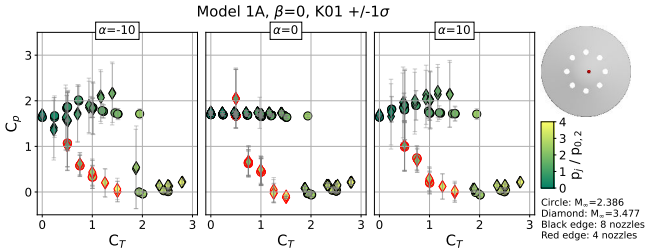

Fig. 11: Model 1A Kulite C_p near heatshield center at $\beta = 0°$.

The influence of nozzle cant angle is illustrated by comparing model 1A and model 1B (Figure 12). Canting the nozzles outward 20° causes C_p near the middle of the heatshield to stay near non-blowing values for all thrust levels. The reason for this is that canting the nozzle also rotates each nozzle's plume, altering the exhaust jet geometry such that the plume never completely blocks the measurement location from external flow. Nozzle canting also results in lower pressure oscillations, except for the 4-nozzle runs at off-reference model attitudes. The effect of moving the nozzles further from the nose (model 1E versus model 1B) are shown in Figure 13, which shows the same overall trends in pressure as with model 1B. Had higher thrust coefficients been possible in the test, the C_p on models 1B and 1E might have reached near zero due to further expansion of the jet plumes and interference with the external flow.

The CobraMRV C_p (Figure 15) is shown to be more sensitive than the HIAD models to both tunnel Mach number and sideslip angle. The differences are due to the nozzle arrangement along the sides of the heatshield and a lack of symmetry that the HIAD model possesses. Non-zero sideslip places one half of the nozzle jet plumes in more direct opposition to the external flow, which blocks the flow and reduces C_p to near zero at the highest thrust.

Figure 16 shows model 1A C_p at a Kulite location outboard of the nozzle radial locations. The trends shown in the plots are typical of all HIAD models, whereby increasing the thrust results in a monotonic reduction in C_p due to the gradual growth of the nozzle

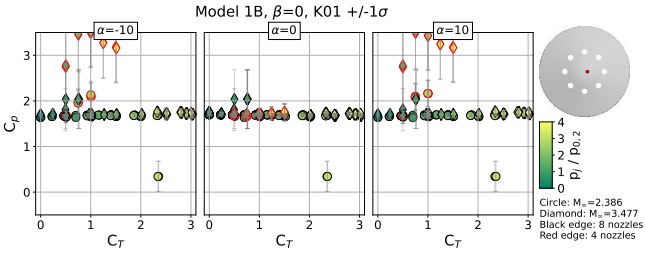

Fig. 12: Model 1B Kulite C_p near heatshield center at $\beta = 0°$.

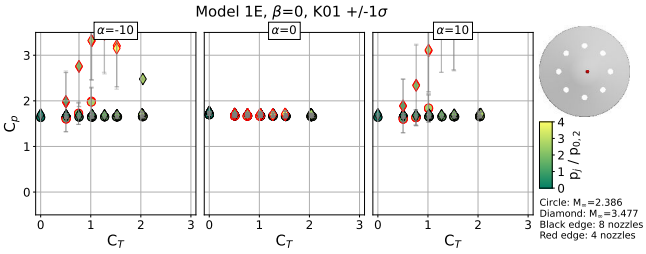

Fig. 13: Model 1E Kulite C_p near heatshield center at $\beta = 0°$.

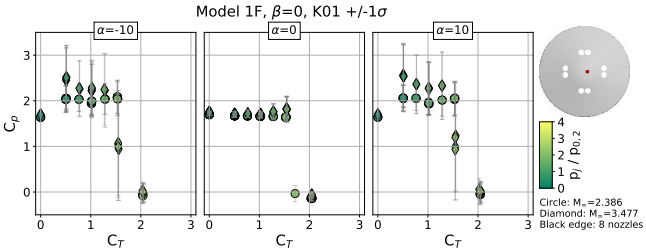

Fig. 14: Model 1F Kulite C_p near heatshield center at $\beta = 0°$.

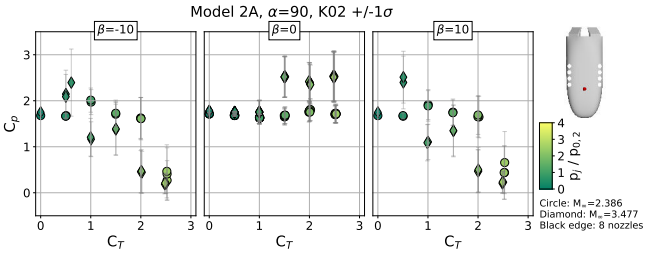

Fig. 15: Model 2A Kulite C_p near heatshield center at $\alpha = 90°$.

plume interference obstructing the external flow. Since the outboard area of the HIAD models is a larger portion of the total heatshield area, the reduction in outboard C_p will be shown in a later section to dominate the overall HIAD aerodynamic interference force.

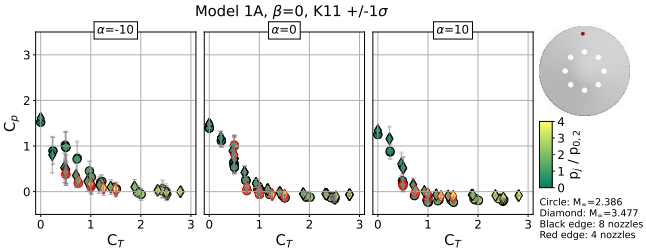

Fig. 16: Model 1A Kulite C_p at heatshield edge at $\beta = 0°$.

Available CFD results are shown against the Kulite data at Mach 2.386 in Figure 17. All CFD codes, regardless of the solution fidelity, produced time-averaged results that in general qualitatively and quantitatively agree with the test data, with the predicted C_p magnitudes mostly well within 0.1 of the test data for all HIAD models. The reduction in C_p is matched at a thrust coefficient of 2.5 for model 1A, as is the increase in CobraMRV pressure at higher thrust. The highest amount of CFD scatter and differences with data for model 2A are at the highest C_T tested, where the standard deviation error bars also are the largest. The CFD temporal standard deviations are predicted for the CobraMRV results at the highest thrust, and the CFD error bars overlap the test data.

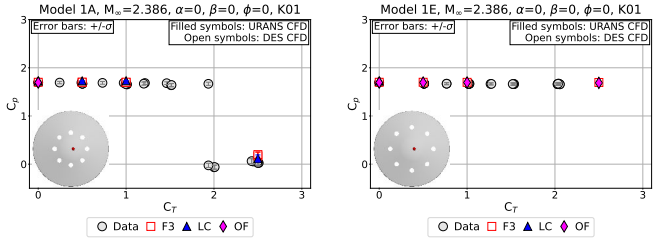

(a) Model 1A, $\alpha = 0°$

(b) Model 1E, $\alpha = 0°$

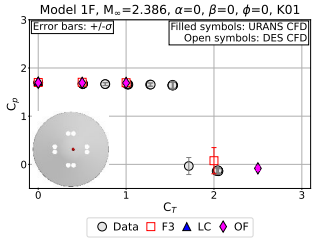

(c) Model 1F, $\alpha = 0°$

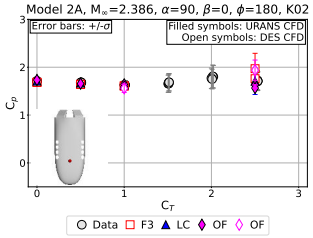

(d) Model 2A, $\alpha = 90°$

Fig. 17: Kulite and CFD C_p near heatshield center at $M_\infty = 2.386$.

Figure 18 shows the effects on stagnation pressure with the models pitched 10° from the reference angle of attack. Pitching the models by 10° places all the nozzles and their plumes in a different orientation relative to the tunnel freestream flow. For example, the plume orientations from nozzle 5 for models 1A/1E and nozzles 5/6 for model 1F are directly impacted by angle of attack. The pressure for model 1F rises above the non-blowing values at intermediate C_T, before decreasing to near zero at the higher thrust coefficients; this phenomenon presumably is the result of nozzle plume pairs interacting with one another. Pitching the CobraMRV model down by 10° has an insignificant effect on the stagnation pressure, which was expected due to the arrangement of the nozzles relative to the pitch direction. Pitching the models by 10° causes temporal fluctuations to increase for models 1A and 1F compared to the data at 0°. The available CFD results qualitatively and quantitatively capture the data trends. The differences between CFD and data are larger than they are at 0° angle of attack, especially for models 1A and 1F; some URANS C_p differences are larger than 0.2 at intermediate thrust coefficients. The limitations of the URANS approach also is seen in some of the predicted standard deviations, especially for model 1F at C_T values of 0.5 and 1; the OVERFLOW results appear to be over-damped, resulting in small unsteady fluctuations.

Figure 19 shows measured and predicted C_p for a HIAD model location near the heatshield edge, and along the pitch plane near CobraMRV model flaps. On the HIAD models, the location is in the wake of one or more nozzles whose expanding plume gradually

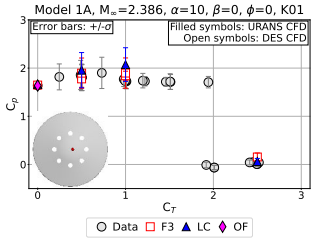

(a) Model 1A, $\alpha = 10°$

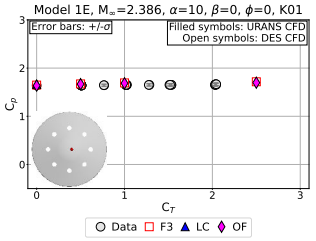

(b) Model 1E, $\alpha = 10°$

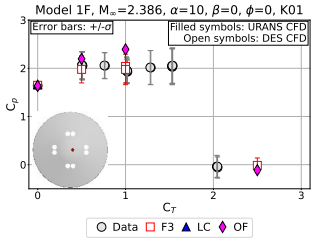

(c) Model 1F, $\alpha = 10°$

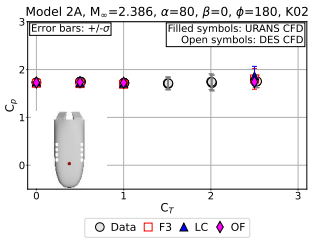

(d) Model 2A, $\alpha = 80°$

Fig. 18: Kulite and CFD C_p near heatshield center with models pitched 10° at $M_\infty = 2.386$.

blocks outboard areas with increasing thrust. The area outboard of the HIAD nozzles constitutes a large portion of the heatshield area, which makes that area important for SRP aerodynamic interference behavior. The trends in pressure coefficient from the test and CFD results for all HIAD models are similar, whereby the C_p gradually decreases with increasing thrust coefficient, asymptotically reaching values slightly below zero at the highest thrust level. The end result on aerodynamic interference force is shown later in the paper. The CobraMRV test and CFD results are similar to the stagnation results, where C_p remains near the non-blowing value at the lower Mach number, and increases at the higher Mach number, much like the stagnation pressure. The similarity in the results to those from the middle of the heatshield is due to the heatshield shape and arrangement of the nozzles along the sides of the heatshield.

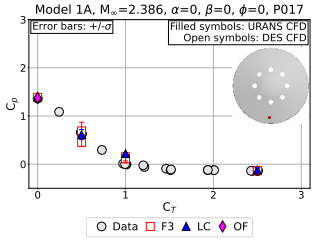

(a) Model 1A

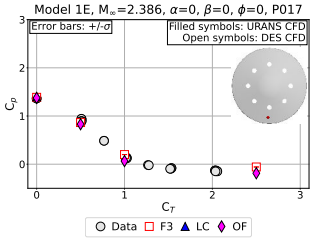

(b) Model 1E

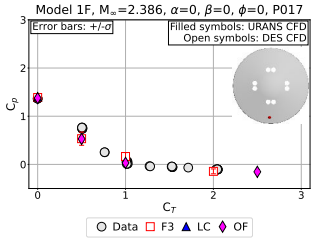

(c) Model 1F

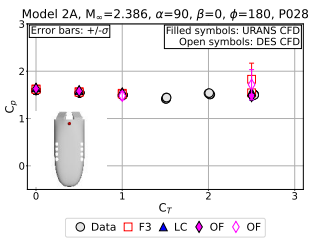

(d) Model 2A

Fig. 19: Tap and CFD C_p at heatshield edge at $M_\infty = 2.386$.

The same data are shown for the models pitched 10° in Figure 20. On HIAD models 1A and 1E, the C_p plateaus somewhat at thrust coefficients between 0.25 and 0.75, then continues to decrease at higher thrust. Again, all CFD results generally track the test data, except for model 1F at intermediate thrust, where significant pressure unsteadiness is predicted using DES methods. The measured and predicted CobraMRV pressures are in good agreement for the steady values, but URANS does not predict the unsteadiness seen in the DES CFD solutions.

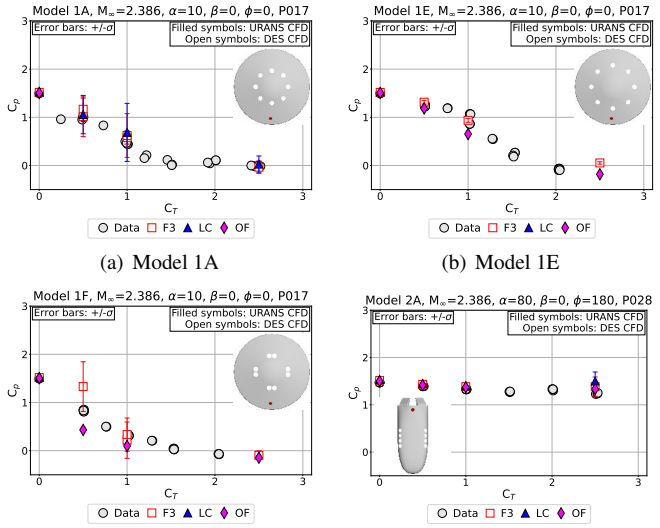

(a) Model 1A (b) Model 1E

(c) Model 1F (d) Model 2A

Fig. 20: Tap and CFD C_p at heatshield edge with model pitched 10° at M_∞ = 2.386.

5.3. Pressure Sensitive Paint

There were several model changes that involved changing nozzle configurations during the test campaign. The CobraMRV model only involved one nozzle change, whereas changes involving the HIAD nozzles were completed several times between configurations. During these model changes, the PSP on the heatshield was damaged. Even during initial installation of HIAD model 1A, some paint chipped off near the nozzle inserts and fasteners. In hindsight, after each model change, the existing PSP layer should have been removed with acetone and a new coating applied. In light of the damaged PSP, results are shown only for HIAD model 1A and the CobraMRV model.

Measured and predicted heatshield C_p distributions are shown in Figure 21. HIAD model 1A results at thrust coefficients of 0.5 and 2.5 illustrate that the CFD qualitatively matches the PSP data. There are indications of artifacts in the PSP data, due to filler material at nozzle fastener locations and paint damage. The plume interference first reduces C_p outboard of the nozzles, then over the entire heatshield at higher thrust, consistent with the discrete pressure data.

Non-blowing and blowing CobraMRV results are summarized in Figure 22. Non-blowing pressure is consistent between PSP data and all available CFD results, as expected. There are some CFD variabilities at the thrust coefficient of 2.5, where the LOCI-CHEM URANS result is compared to the FUN3D and OVERFLOW DES results. The URANS pressure distribution is somewhat broader across the width of the heatshield, compared to the DES pressures.

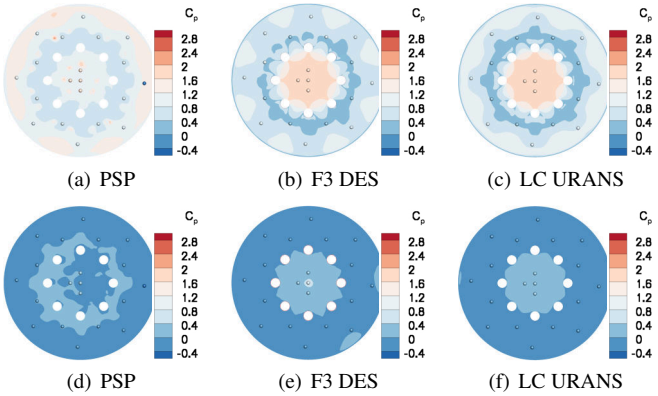

(a) PSP (b) F3 DES (c) LC URANS

(d) PSP (e) F3 DES (f) LC URANS

Fig. 21: HIAD model 1A C_p: M_∞ = 3.477, α = 0°, C_T = 0.5 (top) and 2.5 (bottom).

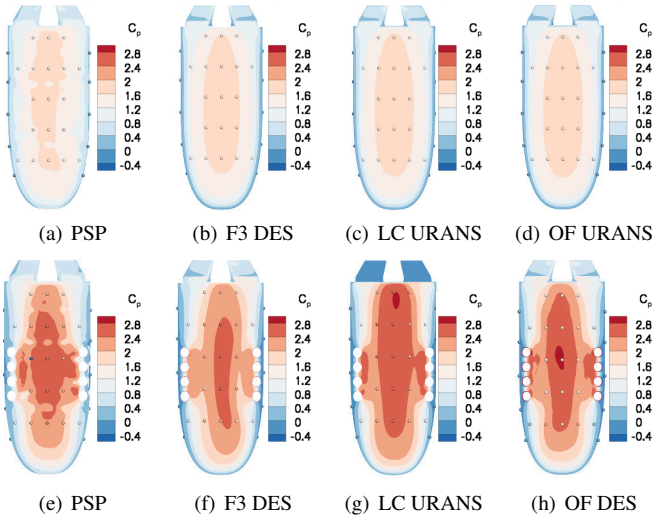

(a) PSP (b) F3 DES (c) LC URANS (d) OF URANS

(e) PSP (f) F3 DES (g) LC URANS (h) OF DES

Fig. 22: CobraMRV model 2A C_p: M_∞ = 2.386, α = 90°, C_T = 0 (top) and 2.5 (bottom).

5.4. Aerodynamic Interference Force Coefficients

The overall forces during SRP are a combination of those generated by engine thrust (prop) and by aerodynamic interference (aero):

$$\vec{F}_{total} = \vec{F}_{prop} + \vec{F}_{aero} \quad (1)$$

In the absence of balance data, aerodynamic forces were derived for HIAD 1A and CobraMRV 2A models by integrating C_p over the PSP-covered heatshields. Figure 23 shows the primary HIAD model 1A force coefficient ($C_{F,x}$) and available CFD results. The general trend for both angles of attack is that, as C_T increases, $C_{F,x}$ gradually decreases due to blockage from the expanding plumes. This result is consistent with the trends shown for the discrete pressure; when C_p approaches zero, first on the heatshield edge (conical flank) and then on the spherical nose, so does the aerodynamic force coefficient. All CFD results show the same overall trends as the data, with higher differences seen near a C_T of 0.5. Previously, CFD pressure coefficients were shown to be lower than measured values for static locations outboard of the nozzles at C_T = 0.5.

Figure 24 summarizes the CFD results for other HIAD models, for which reliable PSP data do not exist, and the CobraMRV model.

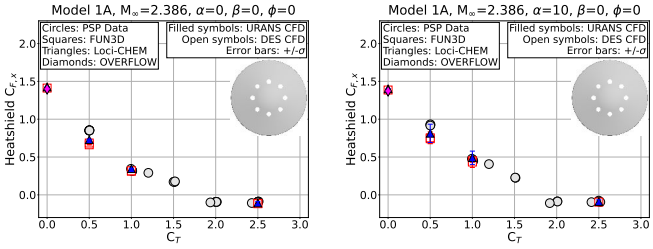

(a) $\alpha = 0°$ (b) $\alpha = 10°$

Fig. 23: HIAD model 1A $C_{F,x}$ at $M_\infty = 2.386$ and $\beta = 0°$.

Model 1B, with nozzles canted 20°, is predicted to experience decreasing $C_{F,x}$ with increasing thrust, but the force coefficient stays above zero for C_T of 2.5, unlike for model 1A. Among all HIAD models, the highest $C_{F,x}$ values are predicted for model 1E, due to the nozzle cant angle and location resulting in a larger area of higher C_p. At SRP flight conditions, C_T would continue to decrease with time due to dynamic pressure decreasing at lower Mach numbers, assuming thrust is not throttled. Therefore, aerodynamic drag may eventually disappear at lower Mach numbers, which would allow thrust-only trajectory simulations until landing.

The CobraMRV force coefficient ($C_{F,z}$) trends generally match the trends in the discrete pressure and PSP data at the lower Mach number of 2.386. $C_{F,z}$ is relatively insensitive to thrust coefficient, in agreement with the discrete pressure data shown in Figure 15. Again, the CFD results are mostly in family with each other and with the test-derived data, with the largest variation between solvers at a C_T of 2.5 on the CobraMRV model.

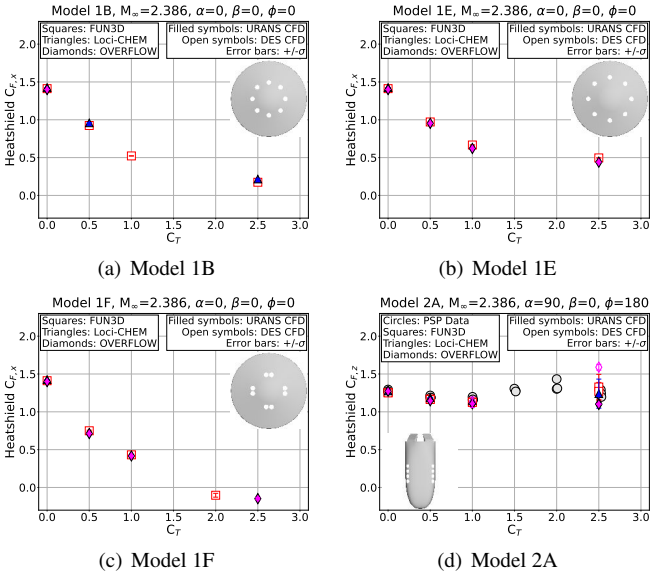

(a) Model 1B (b) Model 1E

(c) Model 1F (d) Model 2A

Fig. 24: HIAD $C_{F,x}$ and CobraMRV $C_{F,z}$ at $M_\infty = 2.386$.

6. SUMMARY

Valuable wind tunnel data were collected to understand SRP physics on NASA Mars powered descent vehicle concepts, and to continue building CFD expertise. Different nozzle parameters were investigated for the HIAD models, with cant angle and location influencing how surface pressure responds to thrust and model attitude. For future SRP wind tunnel testing, the following considerations should be made. First, flow-through balance designs should continue to be developed that would allow reliable direct force measurement in a challenging thermal environment. Second, testing using something other than HPA should be considered, such as heated ethane or small engines if possible, to better represent hot-gas combustion plumes. Testing and CFD at lower supersonic and transonic conditions would allow trends to be extended to lower Mach numbers for EDL systems analysis. On the CFD side, analysis at various levels of fidelity show promising results in capturing qualitative and quantitative data trends. RANS and higher-order analyses should be continued to better understand the strengths (time-averaged heatshield pressures) and weaknesses (unsteady pressures using RANS) of each approach. Applying those same methods to full-scale Mars conditions would help understand how the wind tunnel data and CFD lessons may or may not apply to flight conditions. For instance, it should be investigated whether rearranging the engines on the heatshield to maintain some level of aerodynamic drag benefits the overall system (e. g. propellant mass, maximum thrust-to-weight). Future testing should use the latest available information on full-scale vehicle concepts, and the trends continuously used in integrated Mars EDL analysis.

7. REFERENCES

[1] Cianciolo, A. D., Korzun, A., Edquist, K., Samareh, J., Sostaric, R., Calderon, D., and Garcia, J. A., "Human mars entry, descent and landing architecture study: Phase 3 summary," AIAA Paper 2020-1509, January 2020.

[2] Korzun, A., Canabal, F., Tang, C., Childs, R., Van Norman, J., Tynis, J., and Bibb, K., "Powered descent aerodynamics for low and mid lift-to-drag human mars entry, descent and landing vehicles," AIAA Paper 2020-1510, January 2020.

[3] Edquist, K. T., Falman, B. E., Burns, D. E., Watkins, A. Neal, Pham, H. T., and Houlden, H. P., "Testing of two mars powered descent vehicle concepts in the langley unitary plan wind tunnel," AIAA Paper 2024-3970, July 2024.

[4] Edquist, K. T., et al, "Computational analysis of two mars powered descent vehicle concepts tested in the langley unitary plan wind tunnel," AIAA Paper 2024-3971, July 2024.

[5] Matsuno, K. V., Childs, R. E., Stremel, P. M., Garcia, J. A., and Pulliam, T. H., "Comparison of overflow computational and experimental results of the cobramrv mars entry vehicle concept during supersonic retropropulsion," AIAA Paper 2024-3972, July 2024.

[6] Halstrom, L. D., Pulliam, T. H., Childs, R. E., and Stremel, P. M., "Comparison of overflow computational and experimental results for a blunt mars entry vehicle concept during supersonic retropropulsion," AIAA Paper 2024-3972, July 2024.

[7] Berry, S. A., Rhode, M. R., and Edquist, K. T., "Supersonic Retropropulsion Validation Experiment in the NASA Langley Unitary Plan Wind Tunnel," *Journal of Spacecraft and Rockets*, vol. 51, no. 3, pp. 664–679, 2014.

[8] Childs, R. E., et al, "Flow characterization of the nasa langley unitary plan wind tunnel, test section 2: Computational results," AIAA Paper 2021-2963, August 2021.

[9] Burns, D. E., Parker, P. A., Cagle, C. M., Toro, K. G., Kleb, B. and Hawke, V. M., "New flow-through wind-tunnel balance for retropropulsion testing," *Journal of Spacecraft and Rockets*, vol. 59, no. 6, pp. 1926–1933, November-December 2022.